Optical cavities and quantum emitters

Koks, C.

2

MICROCAVITY RESONANCE CONDITION, QUALITY FACTOR, AND MODE VOLUME ARE DETERMINED BY DIFFERENT PENETRATION DEPTHS

The penetration depth in a Distributed Bragg Reflector (DBR) co-determines the resonance condition, quality factor, and mode volume of DBR-based microcavities. Recent studies have used an incomplete description of the penetration depth and incorrect equations. We present a complete analysis that involves three different penetration depths. We also present a series of experiments on microcavities to accurately determine the frequency and modal penetration depth of our DBRs and compare these results with theoretical predictions. The obtained results are relevant for anyone who models a DBR as an effective hard mirror if lengths of the order of the wavelength are relevant, as is the case for microcavities.

C. Koks and M. P. van Exter, Opt. Express 29, 6879-6889 (2021)

2.1. INTRODUCTION

Small mode volume cavities have been used for numerous applications such as quantum information processing with individual atoms [42] and lab-on-a-chip sensors [44]. These microcavities typically consist of two highly reflective Distributed Bragg Reflectors (DBR) which can trap light in a small mode volume and thereby increase the light-matter interaction. When microcavities get smaller [45] the penetration depth in the mirrors becomes important. DBRs are also used in many other applications [46] and even exist in nature, in the form of intricate photonic crystals [47].

DBR-based microcavities are often modeled as cavities with two hard mirrors spaced by a cavity length that is extended by the penetration depths of the DBRs. This model is then used to calculate the resonance condition, quality factor and mode volume. However, the optical penetration in the DBRs is more subtle than this simple model suggests. In the literature, the penetration depth in DBRs is ambiguously defined due to this simplified model [30–32, 44, 48–50].

This chapter will solve these issues by introducing multiple (frequency, modal, and phase) penetration depths and by explaining when these are relevant. The first part of the chapter presents a theoretical description that aims to provide physical insight into the origin of the various penetration depths. It also links them to the optical properties of a microcavity. The second part presents measurements of the penetration depth in two

types of microcavities. Measurements on the frequency tuning of the modes in a planar cavity yield the frequency penetration depth. Measurements on the transverse mode splitting in a plano-concave cavity yield the modal penetration depth. We compare these two results with each other and with theoretical predictions.

2.2. OPTICAL PENETRATION IN DBRS

We consider the reflection of light from a thick, lossless, planar DBR. The alternating layers have refractive indices n_L and n_H for the low and high index material and layer thicknesses d_L and d_H such that $n_L d_L = n_H d_H = \lambda_c/4$ for vacuum resonance wavelength λ_c. Light is incident from a medium with index n_{in} (typically air with $n_{in} = 1$).

The most prominent feature of DBRs is the existence of a stopband, or bandgap, which is a frequency range where light cannot propagate and where a thick lossless DBR reflects all incident light. The full spectral width of the stopband is [51, 52]

$$\Delta\omega_{gap} = \omega_c \frac{4}{\pi} \arcsin\left(\frac{n_H - n_L}{n_H + n_L}\right) \approx \omega_c \frac{2}{\pi} \frac{\Delta n}{\overline{n}} \tag{2.1}$$

where $\omega_c = 2\pi c/\lambda_c$ is the resonance frequency. The approximation is valid for small to modest index contrast, where $\Delta n \equiv n_H - n_L \ll \overline{n}$ with average index $\overline{n} = (n_L + n_H)/2$. [52]

At resonance, in the center of the stopband, the forward-propagating field decays exponentially into the DBR, such that its amplitude decreases by a factor n_L/n_H per DBR pair [51, 52]. The associated $1/e$ penetration depth L_I of the optical intensity is

$$L_I = \frac{1}{2}\left(\frac{\lambda_c}{4n_L} + \frac{\lambda_c}{4n_H}\right) / \ln\left(\frac{n_H}{n_L}\right) \approx \frac{\lambda_c}{4\Delta n}. \tag{2.2}$$

Note that the division symbol in the central expression in Eq. (2.2) was accidentally forgotten in Eq. (2) of our paper [53]. The approximation again applies to the limit of small index contrast, $\Delta n \ll \overline{n}$.

It seems natural to call L_I "the penetration depth" of the DBR and to model the DBR as an effective hard mirror positioned at a distance L_I behind the front surface of the DBR. But this is wrong for several reasons. First and most important, there is no single position at which a hard mirror can mimic all reflection properties of the DBR simultaneously. Below we will argue that one actually needs three different penetration depths to mimic either (i) the reflection phase, or (ii) the time delay upon reflection, or (iii) the imaging of a focused beam upon reflection. Second, these penetration depths depend on the refractive index n_{in} of the incident medium. Finally, they also depend on whether the DBR starts with a high-index layer (H-DBR) or a low-index layer (L-DBR). Only if one considers the time delay upon reflection from a H-DBR does one obtain the easy "natural" result $L_\tau = L_I$ (see below).

Figure 2.1 shows the calculated frequency dependence of the reflectivity $|r|^2$ and reflection phase φ at normal incidence for a typical DBR, similar to the ones used in our experiments. This figure shows that the reflectivity is approximately constant inside the stopband. The interesting physics is contained in the reflection phase $\varphi(\omega)$, which is defined relative to the front facet and scales as $\varphi \propto (\omega - \omega_c)$. The insets show the physical origin of this phase change: the node of the standing wave, which resides at the DBR surface at resonance, shifts into ($\varphi > 0$) or out of ($\varphi < 0$) the DBR at frequencies $\omega > \omega_c$ and

$\omega < \omega_c$, respectively. Note the deviations from this linear behavior towards the edges of the stopband, where the maximum shift is approximately half a layer thickness for an H-BDR (see Appendix 2.A.).

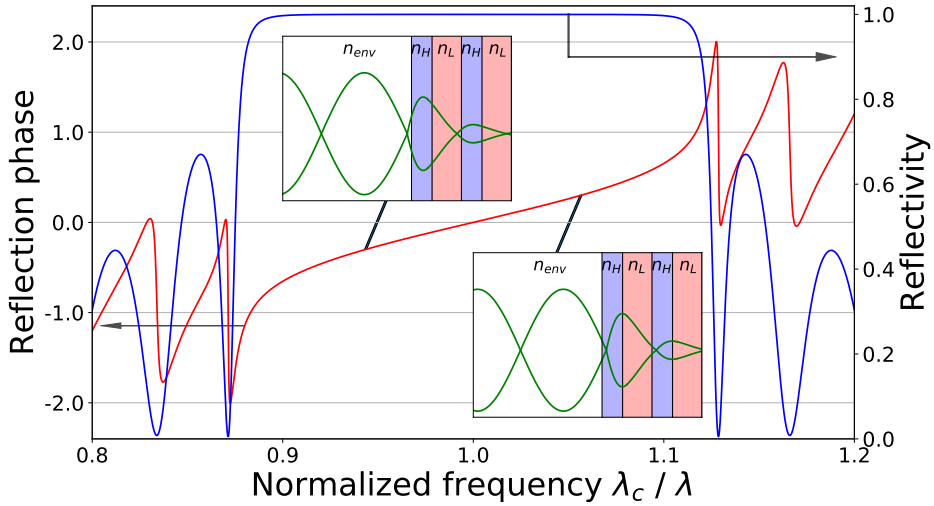

Figure 2.1: Calculated reflectivity (blue) and reflection phase (red) of DBR versus frequency, normalized to the center frequency. The DBR starts and ends with high-index material, comprises 31 layers with $n_L = 1.46$ and $n_H = 2.09$, is deposited on a n_L substrate and embedded in air ($n_{in} = 1$). The insets sketch how the nodes in the electric field shift into/out of the DBR when the frequency is higher/lower than the center frequency.

To describe the reflection of a general (non-monochromatic non-planar) beam of light, we decompose the incident light in its Fourier components. We label these components by their frequency ω and transverse wavevector $k_\rho = k_{in} \sin\theta_{in}$, where $k_{in} = n_{in} k_0$ is the wavevector in the incident medium and $k_0 = 2\pi/\lambda_0$ and λ_0 are the wavevector and wavelength in vacuum. Each monochromatic plane-wave component will reflect with its own reflection amplitude $r(\omega, k_\rho) \exp\{[i\varphi(\omega, k_\rho)]\}$.

Inside the stopband, $r(\omega, k_\rho)$ is approximately constant and equal to $r_c \approx \pm 1$. The optical field has an anti-node ($r_c = 1$) at the front facet for a L-DBR and a node ($r_c = -1$) for a H-DBR. For frequencies near ω_c and small incident angles, the reflection phase $\varphi(\omega, k_\rho)$ can be approximated by [54–56]

$$\begin{aligned} \varphi(\omega, k_\rho) = 2k_{in} L_\varphi &\approx \frac{\partial \varphi}{\partial \omega}(\omega - \omega_c) + \frac{1}{2}\frac{\partial^2 \varphi}{\partial k_\rho^2} k_\rho^2 \\ &= 2(k_{in} - k_c) L_\tau - \frac{k_\rho^2}{k_{in}} L_D \,. \end{aligned} \tag{2.3}$$

The approximation is a Taylor expansion, where $\partial\varphi/\partial k_\rho = 0$ due to mirror symmetry. The final equation defines the frequency penetration depth L_τ and the modal penetration depth L_D in terms of derivations of the reflection phase. We prefer to call L_τ the fre-

quency penetration depth, whereas others have called it the phase penetration depth [54], because our name links L_τ with frequency tuning (see below).

The frequency penetration depth $L_\tau = c\tau/(2n_{in})$ quantifies the group delay $\tau = \partial\varphi/\partial\omega$ that an optical pulse experiences upon reflection from a DBR when its optical spectrum fits well within the stopband. A hard mirror positioned at a distance L_τ in the incident medium will produce the same group delay and will hence mimic the time/frequency properties of the DBR.

The modal penetration depth L_D quantifies the imaging properties of the DBR reflection. A hard mirror positioned at a distance L_D in the incident medium will reflect light with the same angle dependence and will hence produce the same imaging as the DBR. Note that the reflection of the DBR depends on angle because the center of the stopband shifts to higher frequencies at non-zero angles of incidence as $\omega_c(k_\rho) - \omega_c(k_\rho = 0) \propto k_\rho^2$. This dependence results in the relation $L_D/L_\tau = \beta = n_{in}^2(n_L^{-2} + n_H^{-2})/2 \approx (n_{in}/\overline{n})^2$ [54]. This relation is intuitive, because L_τ is associated with a time delay, which scales with $\overline{n}/n_{in}$, and L_D is associated with an imaging shift, which scales with $n_{in}/\overline{n}$ (see Appendix 2.C.). With the factor β we can rewrite the phase penetration in Eq. (2.3) depth in terms of L_τ,

$$L_\varphi = \left(\frac{k_{in} - k_c}{k_{in}} - \frac{1}{2}\beta\theta_{in}^2\right) L_\tau. \tag{2.4}$$

This equation shows that small angles θ_{in} only have a small impact on L_φ, because β is typically small for $n_{in} = 1$.

The phase penetration depth $L_\varphi = \varphi/(2k_{in})$ that we define in Eq. (2.3) is new in literature. We explicitly define this quantity because L_φ determines the resonance condition of DBR-based microcavities, rather than L_τ or L_D; see Eqs. (2.6) and (2.8) below. L_φ also determines the locations of the anti-nodes in the microcavities, where light-matter coupling is maximal. Equation (2.4) shows that $L_\varphi(\omega)/L_\tau = (\omega - \omega_c)/\omega$ at normal incidence for $n_{in} = 1$.

Babic et al. [55] have calculated the frequency penetration depth $L_\tau = c\tau/(2n_{in})$, using transfer matrices. Although Babic et al. only analyzed so-called "matched DBRs", where all reflections interfere constructively, their results

$$\tau = \left(\frac{n_{in}}{n_H}\right)\left(\frac{n_H}{n_H - n_L}\right)\left(\frac{\pi}{\omega_c}\right) \text{ (H-DBR)} \quad \text{or} \quad \tau = \left(\frac{n_L}{n_{in}}\right)\left(\frac{n_H}{n_H - n_L}\right)\left(\frac{\pi}{\omega_c}\right) \text{ (L-DBR)} \tag{2.5}$$

also apply to the general case. The delay time τ is different for high-index and low-index DBRs due to the interference of the reflection from the first interface of the DBR with the reflections from the bulk (see Appendix 2.B.). We have checked both equations (2.15) with numerical calculations based on transfer matrices (see Appendix 2.A.). Brovelli et al. [57] have performed similar calculations, using coupled-mode theory for DBRs with small index contrast. Their results agree with the ones obtained by Babic [55] in the limit of small index contrast (see Supplement 2.B.).

We like to finish this section by noting that the theory described above is based on several assumptions. First of all, the truncated Taylor expansion in Eq. (2.3) is valid only for small frequency detunings and small angles. Second, we have neglected polarization effects. These will play a role at larger angles where the Fresnel reflection coefficients depend on polarization. As a result, the spectral width of the stopband will increase for s-polarized light and decrease for p-polarized light. Finally, we have neglected dispersion

effects. For our DBRs and wavelength, the ratio between the group and phase refractive index is ≈ 1.013 for the SiO_2 layers and ≈ 1.058 for the Ta_2O_5 layers [58]. The combined effect of dispersion, as a weighted average of these values, results in a modest 3 % reduction of the spectral width of the stopband and an associated 3 % increase of the penetration depth. We have neglected this effect in most of our analysis.

CONSEQUENCES FOR CAVITY RESONANCES

The resonances of any optical cavity are determined by the condition that the round-trip phase delay is a multiple of 2π. For a cavity with two planar DBRs illuminated at normal incidence this results in

$$2k_{in}L_{cav} + \varphi_1 + \varphi_2 = n_{in}k_0(2L_{cav} + 2L_{\varphi 1} + 2L_{\varphi 2}) = q\,2\pi \tag{2.6}$$

where L_{cav} is the distance between the front facets of the two DBRs and φ_1 and φ_2 are the reflection phases of the two DBRs (note that $\varphi = 2k_{in}L_\varphi$). The longitudinal mode number q counts the number of half wavelengths in the standing wave pattern between the mirrors. This number q is integer when both mirrors are either H-DBR or L-DBR and hence both have an anti-node or node close to their front facet. For cavities with one H-DBR and one L-DBR we need to replace q by $q + \frac{1}{2}$ to keep q integer and still account for the sign difference in the reflection $r_c = \pm 1$ of the two mirrors.

Now suppose we change the cavity length and measure the resulting change in resonance frequency/wavelength at fixed q. We calculate this change by substituting $L_{cav}(k_0)$ in Eq. (2.6) and taking the derivative of this equation with respect to k_0 to arrive at equation (2.7). In the process we use $d\varphi/dk_0 = 2L_\tau/n_{in}$ in the left equation (2.6) or $L_\varphi(\omega)/L_\tau \approx (\omega - \omega_c)/\omega$ in the middle equation (2.6). When we rewrite the end result in terms of λ we find a normalized slope

$$\lambda\, dL_{cav}(\lambda)/d\lambda = L_{cav} + L_{\tau 1} + L_{\tau 2}\,, \tag{2.7}$$

This equation shows that the relevant penetration depth for a frequency scan is L_τ and not L_φ. The combination $L_{cav} + L_{\tau 1} + L_{\tau 2}$ also determines the quality factor Q of the optical resonances and the associated cavity loss rate ω_0/Q.

The resonance condition of plano-concave cavities differs from that of planar cavities by the so-called Gouy phase. For planar-concave cavities with hard mirrors, the resonant modes are Hermite-Gaussian $TEM_{n,m}$ modes with flat wavefronts at the planar mirror and matched curved wavefronts at the concave mirror. Upon propagation, these modes experience a phase lag relative to a plane wave. This phase lag is proportional to $(n+m+1)$ and to the Gouy phase $\chi_{Gouy} = \arcsin\left(\sqrt{L/R}\right)$ of the fundamental TEM_{00} mode, where L and R are the cavity length and mirror radius.

The resonant optical modes of a planar-concave cavity with DBR mirrors are also $TEM_{n,m}$ modes. Their (round-trip) resonance condition

$$n_{in}k_0(L_{cav} + L_{\varphi 1} + L_{\varphi 2}) - (n+m+1)\chi_{Gouy} = q\,\pi\,, \tag{2.8}$$

again includes the phase penetration depth L_φ of both mirrors. It also includes a Gouy phase that is now given by $\chi_{Gouy} = \arcsin\left(\sqrt{(L_{cav} + 2L_D)/R}\right)$. Note that the relevant penetration depth in this equation is L_D, because the Gouy phase is associated with phase fronts and thereby linked to imaging properties. We assume that the value of L_D for the

curved mirror and the flat mirror are the same, and therefore use $2L_D$. The radius of curvature R is an effective radius, which includes all small variations of the mirror curvature in the fabrication process [59]. The Gouy phase co-determines the Rayleigh range and waist of the cavity modes and hence also the optical mode volume and attainable atom-field interaction.

COMPARISON WITH LITERATURE

A comparison of our results with literature shows that the subtleties of multiple penetration depths are often overlooked. We will give a few examples of how equations would have been different if our theory would have been used.

First, our Eqs. (2.6) and (2.8) show that the resonance condition depends on the phase penetration depth L_φ, which is typically small and zero at resonance. But Eqs. (2) and (3) in ref. [44] state that the resonance condition contains a single wavelength independent penetration depth. The authors later use the same quantity to describe the frequency tuning of the resonances, whereas our Eq. (2.7) shows that frequency tuning depends on the frequency penetration depth L_τ.

Second, our Eqs. (2.6) and (2.7) show that the frequency spacing between consecutive longitudinal modes depends on the frequency penetration depth L_τ. But the authors in [48] determine the longitudinal mode value by taking $q = 2\frac{\partial L_{cav}}{\partial \lambda}$ and hence forget the contribution of L_τ.

Third, our Eq. (2.8) shows that the frequency spacing between the transverse modes depends on the modal penetration depth L_D. Equation (3) in ref. [44] uses the expression $\chi_{Gouy} = \arccos\sqrt{1 - L_{cav}/R}$ for the Gouy phase and hence does not take any penetration into account. Reference [48] makes the same mistake in their Eq. (1). Reference [32] uses the frequency penetration depth in their Eq. (2) for the Gouy phase. But the correct equation should have been $\chi_{Gouy} = \arccos\sqrt{1 - (q\lambda/2 + 2L_D)/R}$ at $L_\varphi = 0$.

Finally, incorrect use of the penetration depths also affects the Purcell effect. Our analysis shows that the Purcell factor F_P depends primarily on the modal penetration depth L_D, as the increase in mode volume due to the field penetration into the DBRs is compensated by a similar increase of the quality factor. The effect of L_D on the Purcell factor is typically small but can still be relevant when the cavity length is order λ. The consequence of using L_τ instead of L_D is a small underestimation of the Purcell enhancement [50].

2.3. METHODS

Our planar and patterned mirrors were produced by Oxford High-Q. The patterned substrate is fabricated with a focused-ion-beam-etching technique that creates a series of high-quality concave structures with typical radii of curvature of 2-20 μm [44, 49, 59]. The SiO_2 substrates were coated with 31 and 35 alternating layers of SiO_2 and Ta_2O_5, to produce two DBRs that both end with high-index material and hence have virtually identical reflection properties. These DBRs have a stopband with a width $\Delta\lambda \approx 150$ nm centered around $\lambda_c = 640$ nm, as expected for a DBR with $n_L \approx 1.46$ and $n_H \approx 2.09$. The transmission of the patterned mirror is $(3.4 \pm 0.2) \times 10^{-5}$ and the transmission of the flat mirror is $(1.1 \pm 0.1) \times 10^{-4}$ at the centre of the stopband. The transmission through the plano-concave cavity is only $\approx 1\%$, due to scattering losses on the mirrors. These losses are not relevant for the analysis presented in this chapter.

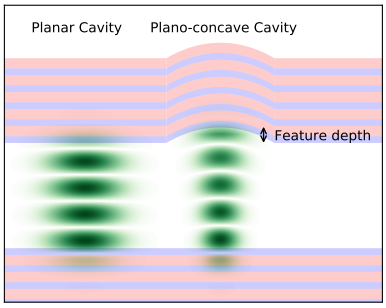

Figure 2.2: Illustration of the planar and plano-concave cavity modes. The blue and red areas correspond to the high and low index materials of the DBR, with a flat mirror at the bottom and a patterned mirror at the top. The green areas indicate standing waves in the cavity. To excite the planar or plano-concave cavity we focus light either on the flat or on the curved part of the patterned mirror. The indentation at the patterned mirror is referred to as "feature depth".

One of the mirrors is fixed while the other mirror can be moved with 6 degrees of freedom on a hexapod system. We align the mirrors to the point where they are parallel and touch each other. This point is referred to as 'touch down'. We scan the mirror position from touch down to over >2 μm distance with sub-nm precision.

The non-linearity of the piezo scan and the point of touch down are determined by measuring the microcavity transmission outside the stopband with a green laser ($\lambda = 520$ nm). A CCD image of the microcavity confirms the parallelism when no fringes are visible. The point of touch down is determined from the part in the scan where the transmitted intensity is constant.

In the next section, we will present accurate measurements of penetration depths on a planar and a plano-concave microcavity, as indicated in the section titles. Figure 2.2 shows that we use the same mirrors in both experiment, but we focus light on different parts. The planar microcavity transmission spectra presented in Fig. 2.3 are obtained with a spatially-filtered Xenon lamp and a fiber-coupled spectrometer. The experimental results on the transverse mode splitting of the plano-concave microcavity, presented in Figs. 2.4 and 2.5, are obtained by measuring the microcavity transmission of a HeNe laser ($\lambda = 633$ nm) with a photo-multiplier tube. The light was coupled in with an $f = 7.5$ mm lens and coupled out with an $f = 8$ mm lens.

2.4. RESULTS

2.4.1. FREQUENCY PENETRATION DEPTH L_τ (PLANAR CAVITY)

In the first experiment, we measure the transmission spectrum $P(\lambda; L)$ of the planar cavity. For each wavelength λ, the transmitted power varies between $P_{min}(\lambda)$ and $P_{max}(\lambda)$ with L. We use these extrema to normalize the transmission spectrum between 0 and 1 and show the results as false-color plot in Fig. 2.3. Due to this normalization, this figure does not show the 4 orders of magnitude difference between the very low transmission (10^{-4}) for

wavelengths inside the stopband and the order unity transmission outside the stopband.

The cavity length is varied from just below touch down (red dashed line indicated by L_{TD}) to a mirror position ≈ 3.6 μm. Below the point of touch down, the cavity length is constant and close to zero. This part is only included to show the derived quantities $L_{cav} = 0$ and L_b (see below).

The slanted lines in the central region of the spectrum show the planar-cavity modes in the stopband. These lines become non-linear towards the edges of the stopband, where the reflection phase φ makes a phase jump, in agreement with the theoretical Fig. 2.1. The planar-cavity modes are labeled by their longitudinal mode number q.

The slanted dashed lines in Fig. 2.3 result from a simultaneous constrained linear fit of the $q = 1-7$ longitudinal cavity modes in the linear part of the stopband (600-680 nm). This fit is heavily constrained and contains only one fit parameter, L_b, because all fit lines are $\lambda/2$ apart and hence cross at the same point L_b for $\lambda = 0$. Small deviations from the fit lines observable for $q = 2-5$ originate from an imperfect correction of the non-linearity of the piezo scan. These fits also allow us to extrapolate to the virtual $q = 0$ mode. At the center wavelength, where $\varphi = 0$, the $q = 0$ line coincides with the point $L_{cav} = 0$, indicated by the middle red dashed line.

The key result in Fig. 2.3 is the observation that the $q = 0$ mode is also slanted or, equivalently, that the point L_b does not correspond to $L_{cav} = 0$. The distance between these points, indicated by the arrow in Fig. 2.3, yields the frequency penetration depth $L_\tau = 0.28 \pm 0.02$ μm; see Eqs. (2.6) and (2.7) for theory. The uncertainty estimate is based on a comparison between results from different measurement series and different methods of analysis, both manually and by computer. Note that the analysis presented above was based on the reasonable assumption that the first mode after touch down is the $q = 1$ mode. This assumption yields a distance 0.14 ± 0.02 μm between touch down and zero cavity length. If the first mode would have been $q = 2$, this would have led to a much larger distance of 0.46 ± 0.02 μm and an unrealistically low value of $L_\tau = 0.12 \pm 0.02$ μm (see discussion below).

2.4.2. MODAL PENETRATION DEPTH L_D (PLANO-CONCAVE CAVITY)

In the second experiment, we measure the transmission of a HeNe laser through a plano-convave cavity while scanning the cavity length. Each group of transmission peaks contains the fundamental TEM_{00} mode and multiple high-order TEM_{nm} modes. The wavelength of the HeNe ($\lambda = 633$ nm) is close enough to the center wavelength ($\lambda_c = 640$ nm) to neglect the phase penetration depth (theory predicts $2L_\varphi \approx -0.01$ μm).

Figure 2.4 shows the measured splitting ΔL between each transverse higher-order mode (indicated by $n + m > 0$) and the associated fundamental mode ($n + m = 0$) as a function of mirror position. We measured these splittings for 7 groups of modes, of which the first three ($q = 3, 4, 5$) are indicated by dashed black lines. Below, we will explain why we start counting from $q = 3$.

The solid curves are based on a simultaneous fit of all measurements using two fit parameters: the mirror radius R and the position L_a of full degeneracy of the transverse modes. Our fit yields $R = 10.7 \pm 0.1$ μm and $L_a = 0.26 \pm 0.03$ μm (indicated by the left red dashed line). Figure 2.4 shows that these estimates require a serious extrapolation of the data. The computer-generated error bars in Fig. 2.5 are based on statistical errors only and might thus be optimistic (0.03 μm statistical error in L_a) as they do not take systematic

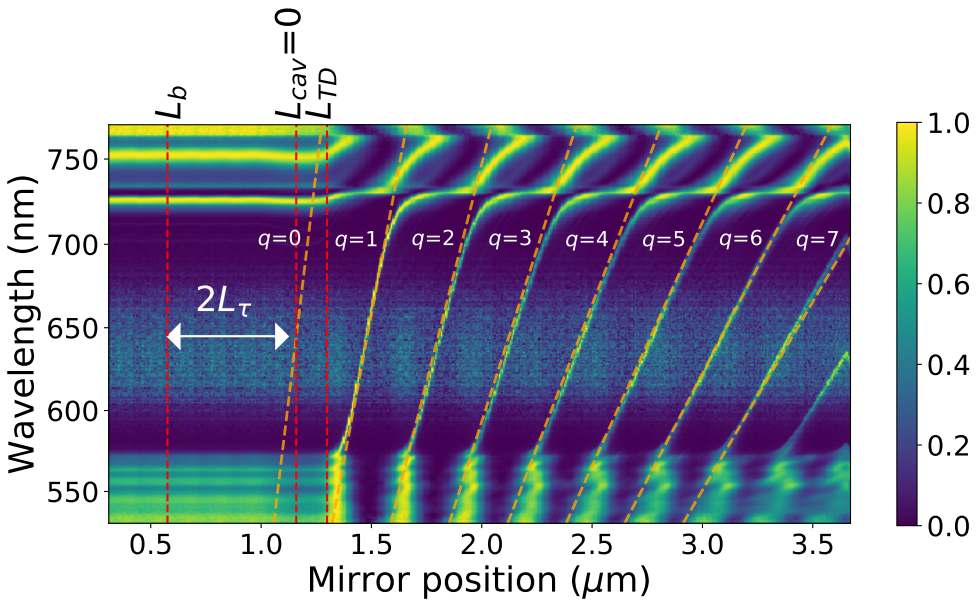

Figure 2.3: False-color plot of the normalized transmission spectrum for a planar cavity. We scan the mirror position from 1.0 to >3.6 μm, which includes the point of 'touch down' (vertical line labeled L_{TD}) and repeat the spectra below 1.0 μm for aesthetic reasons. The slanted lines in the central region of the spectrum show the planar cavity modes in the stopband. These modes are labeled by their mode number q and are fitted with straight (dashed orange) lines. We add the calculated $q = 0$ mode, which per definition intersects the vertical $L_{cav} = 0$ at the central wavelength λ_c. All fits are constrained to cross $\lambda = 0$ at the same mirror position L_b (see text).

errors into account. A possible systematic error could be a deviation of the transverse mode splitting, and the associated Gouy phase, from the simple paraxial theory [60]. In the absence of an alternative theory, we cannot estimate the size of these systematic errors. From an experimental point of view, we can only determine statistical errors to find that errors of multiple measurements on multiple cavities agree with each other (see below).

In Fig. 2.4, we have added an extra (black dotted) curve for the virtual $n + m = -1$ modes. A comparison of Eqs. (2.6) and (2.8) shows that these virtual modes should have the same resonances as the planar cavity modes. By extrapolation of these virtual planar modes to $q = 0$ we find the point $L_{cav} = 0$, indicated as the middle dashed line.

The key result in Fig. 2.4 is the modal penetration depth. Equation (2.8) shows how this value can be obtained from the distance $2L_D$ between the leftmost vertical lines, assuming identical penetration depth in the flat and curved mirror. From the analysis of Fig. 2.4 we thus obtain a measured modal penetration depth $L_D = 0.053 \pm 0.015$ μm.

Finally, we note that the distance between touch down and $L_{cav} = 0$ in Fig. 2.4 is 0.85 ± 0.03 μm. This value is larger than for the planar cavity because it contains the feature depth of the concave mirror (see Fig. 2.2). We have measured this feature depth with an atomic force microscope (AFM) to be 0.62-0.70 μm for different mirrors, i.e. approximately $2 \times \lambda/2$. From this we conclude that the lowest q mode of the plano-concave cavity is $q = 3$, while the planar cavity has $q = 1$. After subtraction of the measured feature depth,

we determine the spacing between the planar parts of the mirrors to be 0.19 ± 0.05 μm at touch down in this new alignment.

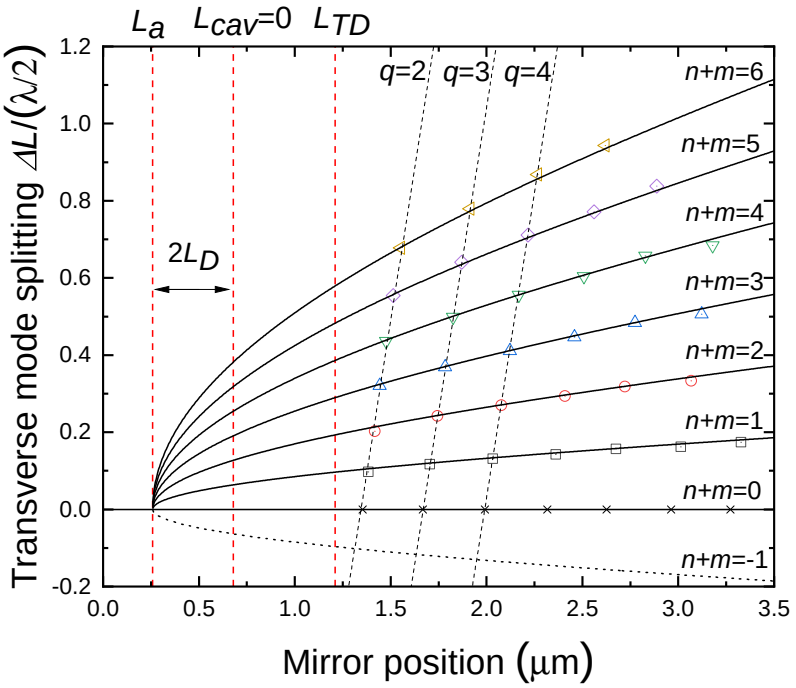

Figure 2.4: Transverse mode splitting versus mirror position L in a plano-concave cavity. This mode splitting is expressed as the displacement ΔL between the resonance of the high-order mode ($n+m=1-6$) and the corresponding fundamental mode ($n+m=0$). The combined fit of these data, depicted as a set of black curves, yield the radius of curvature and a fictitious mirror position L_a where all transverse modes are frequency degenerate. We add the fictitious cavity mode ($n+m=-1$) to compare with the planar cavity and to find $L_{cav}=0$ (see text).

We performed the analysis depicted in Fig. 2.4 on 9 data sets, obtained from 6 different cavities on 2 different days (3 cavities were measured on both days). We only analyzed data sets that contained at least four clearly visible transverse modes. The solid point in Fig. 2.5 shows the fit parameters obtained from Fig. 2.4. The colors of the points indicate measurement series on different days.

The data points in Fig. 2.5 are divided in two groups, corresponding to cavities with $R = 10-11$ μm and $R = 21-23$ μm. The distribution of the data points shows that the modal penetration depth is approximately the same for all cavities and does not depend on mirror radius over the studied range.

The horizontal lines show the weighted average of the modal penetration depth with its intrinsic error $\overline{L_D} = 0.06 \pm 0.02$ μm. This intrinsic error is based on the spread among the measurements, which is slightly larger than the error bars estimated for individual measurements. This estimate only contains statistical errors.

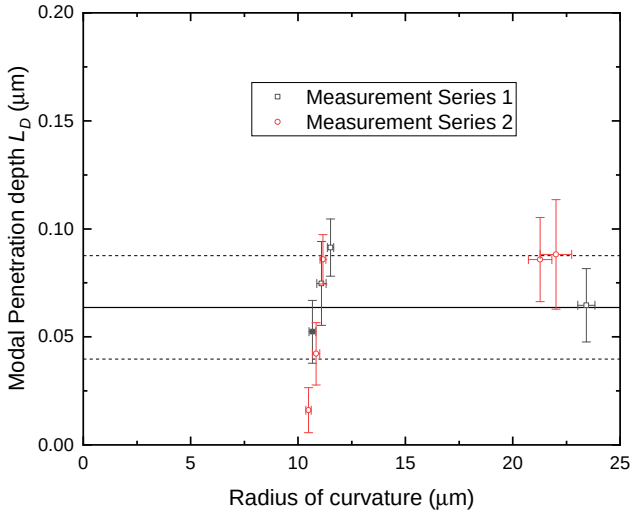

Figure 2.5: Modal penetration depth and radii of curvature for nine measures on various plano-concave cavities. The solid point results from Fig. 2.4. The red and black points are obtained in two measurement series. The horizontal lines show the averaged modal penetration depth and the error range, corresponding to $\overline{L_D} = 0.06 \pm 0.02$ μm.

2.5. DISCUSSION

We start the discussion by comparing experiment with theory. We have measured a frequency penetration depth $L_\tau = 0.28 \pm 0.02$ μm and modal penetration depth $L_D = 0.06 \pm 0.02$ μm. For our H-DBRs, with $n_L = 1.46$ and $n_H = 2.09$, we predict $L_\tau = 0.25$ μm and $L_D = 0.09$ μm. If dispersion is taken into account, we predict $L_\tau = 0.26$ μm and $L_D = 0.09$ μm. Both penetration depths are in reasonable agreement with theory.

The experimental results agree with theory despite several theoretical simplifications. The most crucial simplification seems to be the Taylor expansion of the reflection phase in Eq. (2.3). At large angles of incidence the blue shift of the resonance frequency could bring us into the non-linear regime of the reflection phase, where an additional cubic term increases the effects (see refs. [61, 62]). This scenario sounds reasonable, as the opening angle is ≈ 0.2 rad (e^{-2}) for the fundamental mode at $q = 3$ and much larger for the high-order modes. However, even angles as large as 0.6 rad will shift the resonance frequency only $\Delta\omega_c/\omega_c \approx (1/2)\beta\theta_{in}^2 \approx 5$ % or ≈ 30 nm, which is not enough to reach the non-linear regime. A second simplification lies in the equal treatment of the optical penetration in the flat and curved DBR. This approximation is valid because the penetration depth is much smaller than the curvature of the mirror. A third simplification is the simple paraxial scalar description of the optical field. The mode splittings predicted by an advanced nonparaxial vector description [60] are still small enough to be neglected in our analysis. Finally, we didn't take potential coating inhomogeneities and thickness distortions of the mirrors into account. Small-scale distortions are likely to average out over the mode profile. But large-

scale distortions can deform the transverse modes away from the ideal spherical case and hence result in an incorrect assignment of the radius R and the modal penetration depth L_D [63]. A discussion of all these complications is beyond the scope of the chapter.

In conclusion, we have presented an analysis of optical penetration in DBRs and accurate measurements thereof. Our analysis shows that there are actually three penetration depths which are relevant in different experiments. We have measured the frequency penetration depth L_τ to find that it agrees with theory. We have also measured the modal penetration depth L_D to find that it is much smaller than L_τ, again as expected. Maybe most importantly, we have argued that the effect of optical penetration on microcavity resonances is often misinterpreted. The absolute resonance conditions depend on the reflection phase φ and hence on the phase penetration depth L_φ. The frequency spacing between the longitudinal modes and their quality factor depend on the frequency penetration depth L_τ. The frequency spacing between the transverse modes and their area/cross sections depend on the modal penetration depth L_D. The Purcell factor F_P depends primarily on the modal penetration depth, as the increase in mode volume due to the field penetration into the DBRs is compensated by an increase of the quality factor.

2.A. COUPLED-MODE THEORY AND SHIFT OF (ANTI-)NODES

The main text states that 'the node of the standing wave, which resides at the DBR surface at resonance, shifts into ($\varphi > 0$) or out of ($\varphi < 0$) the DBR at frequencies $\omega > \omega_c$ and $\omega < \omega_c$, respectively. Note the deviations from this linear behavior towards the edges of the stopband, where the maximum shift is approximately half a layer thickness for a H-BDR (see Appendix 2.A.).' In this section, we will prove that statement. We will do so by using the coupled-mode theory formulated e.g. in [51] and applied to DBRs in [51, 57].

We consider the reflection of light from a thick lossless planar DBR illuminated at normal incidence. The alternating layers have refractive indices n_L and n_H, and layer thicknesses d_L and d_H such that $n_L d_L = n_H d_H = \lambda_c/4$ for vacuum resonance wavelength λ_c. The average index $\overline{n}$ is defined via $\overline{n}\Lambda = n_L d_L + n_H d_H$, where $\Lambda = d_L + d_H$ is the periodicity (= thickness per pair). The DBR is embedded in a medium with index $\overline{n}$ and $\Delta n = (n_H - n_L) \ll \overline{n}$ (small index contrast). The DBR starts with the high-index material at position $z = 0$.

We write the optical field $E(z,t) = [A(z)\exp\{[i(\pi/\Lambda)z]\} + B(z)\exp\{[-i(\pi/\Lambda)z]\}]\exp\{(-i\omega t)\}$, where $A(z)$ and $B(z)$ are the slowly-varying amplitudes of the forward and backward traveling wave. Reflection at the periodic interfaces couples forward and backward traveling waves with a coupling rate κ that satisfies the relation $\kappa\Lambda = \Delta n/\overline{n}$ [51, 57]. We define the resonance frequency as ω_c and the resonance wavevector as $k_c = \pi/\Lambda$. We also define a wavevector detuning $\delta = k - k_c = \overline{n}(\omega - \omega_c)/c$ for light with frequency ω, where we neglect dispersion. Upon propagation in the DBR the amplitudes of the waves evolve as [51]

$$\frac{d}{dz}\begin{pmatrix} A(z) \\ B(z) \end{pmatrix} = \begin{pmatrix} i\delta & \kappa \\ \kappa & -i\delta \end{pmatrix}\begin{pmatrix} A(z) \\ B(z) \end{pmatrix} \tag{2.9}$$

Within the stopband, where $|\delta| < \kappa$, the eigenvalues of the propagation matrix are $\pm\gamma = \pm\sqrt{\kappa^2 - \delta^2}$. When we express the detuning as $\delta = \kappa\sin\phi$, this corresponds to $\gamma = \kappa\cos\phi$. In the center of the stopband, at $\delta = 0$, the eigenvalue $\pm\gamma = \pm\kappa$ indicates that the optical field decays at a rate $\kappa = \Delta n/(\overline{n}\Lambda) = 2\Delta n/\lambda_c$ into the DBR. Off-center, the field penetrates

deeper as the decay rate γ decreases by a factor $\cos\phi$. The full spectral width of the stopband, from $\delta = -\kappa$ to κ, is equal to $\Delta\omega_{gap}/\omega_c = 2\kappa/k_c = 2\Delta n/(\pi\overline{n})$, as already mentioned in the main text.

The two eigenmodes of the propagation matrix have $B/A = \pm\exp\{(\pm i\phi)\}$. A decomposition of the incident and transmitted field in these eigenmodes shows that the reflection amplitude of an infinitely thick DBR can be written as

$$\Gamma_0 = \frac{-\kappa}{\gamma - i\delta} = -\exp\{i\phi\}, \tag{2.10}$$

for the reflection at the low-to-high-index interface (at $z = 0$). The reflection at the high-to-low-index interface only differs in sign and is $\Gamma_0 = \exp\{i\phi\}$. At resonance, the reflection amplitude is $\Gamma_0 = \pm 1$, where the plus sign applies to L-DBRs and the minus sign applies to H-DBRs. For off-center frequencies in the stopband, the reflection phase

$$\phi = \arcsin\frac{\delta}{\kappa} = \arcsin\left[\frac{2(\omega-\omega_c)}{\omega_{gap}}\right] = \arcsin\left[\tau_0(\omega-\omega_c)\right], \tag{2.11}$$

where $\tau_0 = 2/\Delta\omega_{gap}$ is the group delay in the center of the stopband. At the edges of the stopband, where $\delta = \pm\kappa$, the reflection phase reaches its limiting values $\phi = \pm\pi/2$. This phase shift corresponds to a shift of the node in the standing wave over $\pm$ 1/8 wavelength or half the thickness of a DBR layer.

The role of dispersion, i.e. the frequency dependence of the refractive indices, is as follows. In the presence of dispersion, the wavevector detuning $\delta = dk/d\omega(\omega-\omega_c) = \overline{n}_{gr}(\omega-\omega_c)/c$, where $\overline{n}_{gr}$ is the weighted average of the group refractive indices of the DBR layers. For our DBRs and wavelength, the ratio $n_{gr}/n = 1.013$ for SiO_2 and 1.058 for Ta_2O_5 [58], which results in a most correction of order 3 %.

We finish this section with two side notes. First, we note that the arcsin-dependence in Eq. (2.11) shows that the phase varies linear with detuning in the center of the stopband but changes faster towards the edges of the stopband. This is in agreement with our observations and simulations. Second, we note that Eqs. (2.10) and (2.11) describe the reflection of a DBR embedded in a medium with index $\overline{n}$. The reflection phase will change when the DBR is embedded in a medium with index $n_{in} \neq \overline{n}$ (see next section).

2.B. EFFECT OF INCIDENT MEDIUM ON FREQUENCY PENETRATION DEPTH L_τ

The main text states that "the reflection phase φ also depends on the ratio $n_{in}/\overline{n}$" and that the "time delay $\tau = d\varphi/d\omega$ is different for high-index and low-index DBRs due to interference of the reflection from the first interface of the DBR with the reflections form the bulk". In this section, we will prove that statement.

We consider an infinitely thick DBR and write the reflection amplitude from the bulk as $\Gamma_0 = \pm\exp\{[i\tau_0(\omega-\omega_c)]\}$ for frequencies in the central (linear) region of the stopband. For the general case $n_{in} \neq \overline{n}$, we add the reflection amplitude r_0 from the first interface c.q. front facet, which is given by the well-known expression $r_0 = (n_{in}-\overline{n})/(n_{in}+\overline{n})$. The interference between the reflection from the front facet and the bulk yields a combined reflection amplitude [52]

$$r = \frac{r_0 + \Gamma_0}{1 + r_0\Gamma_0}. \tag{2.12}$$

It is easy to show that $r = \pm 1$ when $\Gamma_0 = \pm 1$ and that $|r| = 1$ because $|\Gamma_0| = 1$. Hence, we can write $r = \pm \exp\{[i\tau(\omega - \omega_c)]\}$ in the central region of the stopband. We calculate the ratio τ/τ_0 by taking the frequency derivative of equation (2.12) at $\omega = \omega_c$ to find

$$\frac{\tau}{\tau_0} = \frac{1 - r_0^2}{(1 \pm r_0)^2}, \tag{2.13}$$

For H-DBRs, where the minus sign applies as $\Gamma_0(\omega_c) = -1$, this results in $\tau/\tau_0 = n_{in}/\overline{n}$. For L-DBRs, where the plus sign applies as $\Gamma_0(\omega_c) = +1$, this results in $\tau/\tau_0 = \overline{n}/n_{in}$. These final expressions prove Eq. (3) in the main text, which states that

$$\frac{1}{2}\Delta\omega_{gap}\tau \approx \frac{n_{in}}{\overline{n}} \text{ (H-DBR)} \quad \text{or} \quad \frac{1}{2}\Delta\omega_{gap}\tau \approx \frac{\overline{n}}{n_{in}} \text{ (L-DBR)} \tag{2.14}$$

They quantify the influence of the environment on the group delay τ, and the associated penetration depth L_τ. And they show that the penetration in H-DBRs and L-DBRs differs.

For completeness, we note that the above equations were derived from coupled-mode theory and assumed the refractive index contrast in the DBR to be relatively small. Babic et al. [54] have used a transfer matrix approach to analyze the general case of larger index contrast to find

$$\tau = \left(\frac{n_{in}}{n_H}\right)\left(\frac{n_H}{n_H - n_L}\right)\left(\frac{\pi}{\omega_c}\right) \text{ (H-DBR)} \quad \text{or} \quad \tau = \left(\frac{n_L}{n_{in}}\right)\left(\frac{n_H}{n_H - n_L}\right)\left(\frac{\pi}{\omega_c}\right) \text{ (L-DBR)} \tag{2.15}$$

To verify the above prediction, we have performed numerical calculations using the transfer matrix approach. Figure 2.6 shows that τ indeed increases linearly with n_{in} for the H-DBR, but inversely proportional for the L-DBR. The two lines cross at the point where $n_{in} \approx \overline{n}$, where $\tau\omega_c \approx 8.7$, in agreement with the predicted value $\pi\sqrt{n_L n_H}/(n_H - n_L)) = 8.7$.

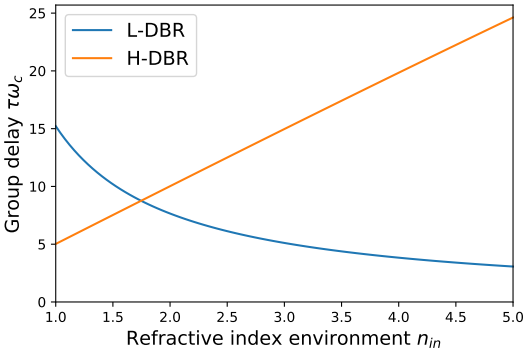

Figure 2.6: Dependence of the group delay on the refractive index of the environment for a H-DBR and L-DBR. The calculated DBR has 30 pairs of layers with $n_L = 1.46$ and $n_H = 2.09$.

2.C. RATIO L_τ AND L_D

The main text stated that the relation between the modal and frequency penetration depth is $L_D/L_\tau = \beta = n_{in}^2(n_L^{-2} + n_H^{-2})/2 \approx (n_{in}/\overline{n})^2$ [54]. We claimed that "this relation is intuitive,

because L_τ is associated with a time delay, which scales with $\overline{n}/n_{in}$, and L_D is associated with an imaging shift, which scales with $n_{in}/\overline{n}$ ". In this section, we will show this analytically and graphically.

The analytic result is derived from the blueshift of the center frequency of the DBR. The reflection $r = \exp\left[i2L_\tau(k - k_c'(\theta_{in}))\right]$ changes with incident angle θ_{in} (in medium n_{in}) because the resonance wavevector $k_c'(\theta_{in})$ changes. This resonance wavevector is determined by the relation $n_L d_L \cos\theta_L + n_H d_H \cos\theta_H = \pi/k_c'(\theta)$ where θ_L and θ_H are the angles in both DBR layers. A Taylor expansion of $\cos\theta_L \approx 1 - \theta_L^2/2 \approx 1 - \theta_{in}^2(n_{in}/n_L)^2/2$ and similar for $\cos\theta_H$ yields a blue shift of the form $k_c'(\theta_{in}) \approx k_c(1 + \beta\theta_{in}^2/2)$, where $\beta = n_{in}^2(n_L^{-2} + n_H^{-2})/2$. A hard mirror positioned at a distance L_D in medium n_{in} has an angle dependent reflection of the form $\exp\{[i2kL_D\theta_{in}^2/2]\}$. A comparison with the DBR shows that this hard mirror mimics the angle dependent reflection from the DBR when $L_D = \beta L_\tau$.

Fig. 2.7 shows the relation between L_τ and L_D graphically. The green lines show the reflection of an incident ray at some penetration depth in the DBR. This ray refracts at the front facet on account of Snell's law, where it bends towards the surface normal for the considered case $\overline{n} > n_{in}$. The red lines/rays show how the apparent position of the reflecting layer, as observed from the n_{in} medium, moves towards the surface normal. This figure thus shows that the modal penetration depth L_D scales with $n_{in}/\overline{n}$. On the other hand, light propagates slower through the high-index material of the DBR than through the low-index environment. Therefore, the frequency penetration depth L_τ of the equivalent hard mirror is larger than the actual penetration depth in the DBR by a factor $\overline{n}/n_{in}$. A comparison of these two prima facie results yields $L_D/L_\tau \approx (n_{in}/\overline{n})^2$, in agreement with the earlier expression for β for small Δn.

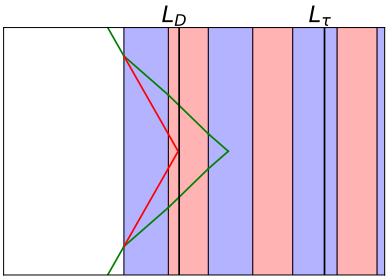

Figure 2.7: Sketch of the reflection of light (green ray) incident at an angle on a DBR for $\overline{n}/n_{in} = 1.94$), which reflect at some penetration depth. The yellow region indicates the environment with n_{in}, the blue and red regions indicate the high (n_H) and low (n_L) index region of the DBR. The red rays indicate the equivalent point of focus if the DBR is replaced by a hard mirror in the refractive index of the environment. The point L_τ is located at L_D/β.